Relationship between ferroelectric polarization and stoichiometry of math xmlns="http://www.w3.org/1998/Math/MathML">msub>mi >HfO/mi>mn>2/mn>/msub>/math> surfaces

Adrian Acosta, J. Mark P. Martirez, Norleakvisoth Lim, Jane P. Chang, and Emily A. Carter

Phys. Rev. Materials **5**, 124417 — Published 29 December 2021

DOI: 10.1103/PhysRevMaterials.5.124417

Physical Review Materials

Relationship between ferroelectric polarization and stoichiometry of HfO_2 surfaces

Adrian Acosta,[1] J. Mark P. Martirez,[1] Norleakvisoth Lim,[1] Jane P. Chang,[1,*]
and Emily A. Carter,[1,2,3,*]

1: Department of Chemical and Biomolecular Engineering, University of California, Los Angeles, Los Angeles, California 90095, United States

2: Department of Mechanical and Aerospace Engineering, Princeton University, Princeton, New Jersey 08544-5263, United States

3: Office of the Chancellor, University of California, Los Angeles, Los Angeles, California 90095, United States

*eac@ucla.edu, jpchang@ucla.edu

Abstract

We used density functional theory to assess the stability of nonpolar tetragonal ($P4_2/nmc$) HfO_2(110) reconstructed surfaces and the effect of polarization on the stability of the corresponding surfaces of polar orthorhombic ($Pca2_1$) HfO_2(001). The models consisted of nine-formula-unit-thick slabs with two-formula-unit surface unit cells. We determined an oxygen-terminated surface reconstruction to be the most stable surface for the nonpolar HfO_2 slab, with one oxygen atom per formula unit on both sides of the slab (1.0-O/1.0-O). For the same surface composition, the ferroelectric displacements in the polar orthorhombic slab result in band bending that leads to the migration of charge carriers to the surface (with sign opposite to that of the surface polarization charge) which metallizes the surface to eliminate or reduce the net out-of-plane dipole. Ionic passivation also is effective at screening the polarization charge, which therefore alleviates band bending leading to stabilization. This is achieved via a nonstoichiometric surface reconstruction, in which the most stable positively polarized side is oxygen-terminated with 1.5

oxygen atoms per formula unit, while the negatively polarized side has one oxygen atom per formula unit (P+:1.5-O/P-:1.0-O). This work establishes a link between the stability of the surface reconstruction and the ferroelectric polarization in HfO_2, which is important for the technological need to control ferroelectric performance at the nanoscale.

I. Introduction

Ferroelectric HfO_2 and HfO_2-based materials have garnered great interest among researchers for next-generation electronic devices, e.g., as a component of ferroelectric random-access memory or ferroelectric field-effect transistors [1-3]. The discovery of ferroelectricity in HfO_2 thin films is fortuitous as hafnia is integrated already in existing silicon technology and its ferroelectric properties can scale well below 10 nm, which circumvents conventional size limitations of perovskite ferroelectrics [4,5]. The robust ferroelectric behavior in nanoscale HfO_2 originates in part from the small depolarization field and energy cost of domain wall formation compared to conventional perovskite ferroelectrics [6]. Researchers ascribed the observed ferroelectricity in thin film HfO_2 to the formation of the polar orthorhombic ($Pca2_1$) phase [7,8]. Although other polar phases of HfO_2 exist in the bulk that are comparable in thermodynamic stability, e.g., $Pmn2_1$ and $Pbca$, as identified by prior computational and experimental investigations [9-14], none of the polar phases is more stable than the monoclinic ($P2_1/c$) HfO_2 phase at low temperatures and pressures [9,15]. In general, multiple reasons may contribute to the emergence of unexpected ferroelectricity in HfO_2, with various studies exploring the effects of dopants [7,16-18], oxygen vacancies [19-22], applied electric-fields [10,12], and strain [10,13,23].

Several prior studies have sought to understand the role of the surface in stabilizing ferroelectricity in HfO_2 thin films. Materlik *et al.* first used a phenomenological model to predict the surface energy and found that one can stabilize ferroelectric HfO_2 grains ($Pca2_1$) below 5 nm [24], although the authors provided no direct empirical or first-principles quantum mechanics evidence. Batra *et al.* studied the role of film thickness [25] and found that at small dimensions (~ 5 nm), certain surface planes may stabilize the polar orthorhombic ($Pca2_1$ & $Pmn2_1$) phases over the nonpolar monoclinic ($P2_1/c$) or tetragonal ($P4_2/nmc$) phases because they yield lower surface energies. However, the above-mentioned studies did not consider the influence of a range of surface stoichiometries on the surface stability of ferroelectric and nonferroelectric HfO_2.

Experimentalists also have investigated interfaces that HfO_2 forms with different electrode materials. The chemistry and concentration of oxygen vacancies at the boundaries depend on the choice of the electrode, which can impact strongly the resulting ferroelectric properties after annealing [26-29]. Recent examples include a study by Szyjka *et al.* finding that exposure to oxygen before deposition of the HfO_2 can control the initial oxidation of a TiN bottom electrode, which directly correlates with the strength of the remnant ferroelectric polarization after annealing [30]. A similar study by Fields *et al.* on $Hf_{1-x}Zr_xO_2$ also highlights that the relative stoichiometry of a TaN_x electrode interfaced with $Hf_{1-x}Zr_xO_2$ impacts the resulting fraction of the orthorhombic phase and strength of the remnant ferroelectric polarization after annealing [31]. During electric field cycling, researchers also observed oxygen vacancy redistributions toward or away from electrodes, leading to stabilization of the orthorhombic phase and increased ferroelectric polarization, the behavior of which strongly depends on the electrode interface chemistry [32-34]. Evidently, the stability of ferroelectricity in HfO_2-based ferroelectrics is sensitive to the interfacial chemistry, and an increased understanding of the relationship between the surface composition and ferroelectric polarization can help guide the design and optimization of devices containing a ferroelectric component.

To explore the effect of polarization on the surface stability and reconstruction, here we look at the closely related paraelectric tetragonal ($P4_2/nmc$) and ferroelectric orthorhombic ($Pca2_1$) HfO_2 phases, where small ferroelectric displacements facilitate a nonpolar to polar transformation between the two phases. Specifically, we investigated the (110) and (001) surfaces of the tetragonal and orthorhombic phases, respectively, where the [110] direction in the nonpolar tetragonal phase corresponds to the [001] direction in the ferroelectric orthorhombic phase, which in turn follows the same direction as the maximum polarization vector in the latter phase.

The presence of a surface/vacuum or air interface presents the need for electrostatic charge compensation mechanisms to avoid electrostatic potential divergence due to unscreened polarization. In a stoichiometric ferroelectric surface, we can expect charge compensation to occur through electronic reorganization (electrons moving from the surface facing negative polarization to the surface facing positive polarization) often leading to surface metallization. This is because the electrostatic potential drives the surface bands to become partially occupied. Formation of nonstoichiometric surfaces also can provide the required electron and hole screening of surface bound charges [35-37]. Thus, because both stoichiometry and polarization themselves contribute to the surface stability, here we decouple the effect of surface polarization and surface reconstruction by first identifying the most energetically stable tetragonal HfO_2 slab surface stoichiometry. We then turn on the polarization in the bulk of the tetragonal slab through the displacements that characterize the tetragonal to orthorhombic phase transition. This enabled us to determine the effect of ferroelectric polarization on surface stability and composition.

II. Methods

A. General parameters in periodic planewave DFT

To model HfO_2 surfaces, we carried out density functional theory (DFT) calculations under periodic boundary conditions using the Vienna *ab initio* simulation package (VASP) version 5.4.4 [38]. We employed the Perdew-Burke-Ernzerhof generalized gradient approximation exchange-correlation (PBE XC) functional [39].

We used Monkhorst-Pack meshes [40] for *k*-point sampling of the Brillouin zone and a kinetic energy cutoff of 800 eV for the plane wave (PW) expansion of the wave functions, in conjunction with the projector augmented-wave (PAW) method [41]. The latter utilizes projector-based potentials to describe the effect of the nuclei and (frozen atomic) core electrons on the outer-core/valence electrons, where the latter's energy and spatial distributions are solved for self-consistently within DFT. Here, we used standard VASP PAW potentials where the 2s and 2p electrons for O and the 5s, 5p, 6s, and 5d electrons for Hf are treated self-consistently. We used Gaussian electronic smearing with a width 0.01 eV to aid the electronic convergence.

B. Bulk simulations

We used a 6×6×4 *k*-point mesh for the two-formula-unit bulk primitive tetragonal cell and a 4×4×4 *k*-point mesh for the four-formula-unit bulk orthorhombic unit cell to maintain comparable *k*-point spacing between the structures. The convergence of the total energy with respect to the *k*-point mesh density and PW kinetic energy cutoff for bulk orthorhombic HfO_2 confirm that our chosen parameters are sufficient to achieve convergence to within 1 meV/atom (**Fig. S1)** [42]. During lattice-vector and atomic-coordinate optimization, all atoms relaxed until the absolute atomic force components were less than 0.001 eV/Å and the absolute value of the pressure was less than 0.03 kbar. The equilibrium lattice parameters thus obtained for the tetragonal phase are a= b= 3.594 Å, c= 5.230 Å, and α, β, γ = 90° whereas for the orthorhombic phase, they are a= 5.274 Å, b= 5.056 Å, c= 5.086 Å, and α, β, γ = 90° (conventionally, the longest axis is assigned as c; here we swap the conventional a and c axes so that the polarization vector is along c, *vide infra*). Hereafter, these bulk vector assignments will be used. The calculated lattice parameters compare well to the measured or previously computed lattice parameters (using VASP with the same PBE XC functional; **Table S1**) [42].

We calculated the bulk orthorhombic structure to be 82 meV/HfO_2 lower in energy than the bulk tetragonal structure, which agrees well with previously reported DFT results also using the PBE XC functional [9]. The phonon densities of states of the bulk structures (**Fig. S2**) confirm these relaxed structures to be energy minima [42]. We present further validation of the method choice with respect to bulk phase transformation thermodynamics in **Table S2** of the SI [42].

We also plot the densities of states for the bulk tetragonal and orthorhombic structures in **Fig. S3** [42]. Despite the good agreement between experiment and DFT-PBE (i.e., DFT with the PBE XC functional) for the structural parameters and relative thermodynamic stability of the HfO_2 phases, their measured band gaps as expected are underestimated by pure DFT eigenvalue gaps [43]. Recall that DFT gaps do not correspond directly to measured band gaps, which involve excited states (for optical or photoemission-derived gaps). DFT only delivers the difference between conduction and valence band edge ground-state energies and formally is expected to yield a lower bound due to the lack of derivative discontinuity of the XC functional [44,45]. For HfO_2, the DFT-PBE eigenvalue gaps are respectively 4.67 and 4.34 eV for the tetragonal and orthorhombic phases whereas the measured band gap of HfO_2 thin films using X-ray photoelectron spectroscopy and spectroscopic ellipsometry is between ~5.25-5.95 eV [46-49]. These large eigenvalue gaps are a consistent lower bound for the actual gap and are sufficient to represent properly the insulating nature of hafnia. Hybrid XC functionals, e.g., B3LYP or B3PW, could be utilized instead, as they often fortuitously achieve eigenvalue gaps that are closer to experimental band gaps, largely through a cancellation of errors (Hartree-Fock gaps being too large and with pure DFT gaps too small, a linear combination can be "just right"). More properly, post-DFT many-body theory (GW, Bethe-Salpeter equation, etc.) can calculate actual band gaps, e.g., for transition-metal-based ferroelectrics [50-53]. However, both hybrid DFT and post-DFT many-body theories are significantly more computationally expensive than pure DFT, which is sufficient for our purposes here.

C. Surface simulations

We constructed the HfO_2 slab supercell structures composed of approximately nine formula units of HfO_2 layers (17 - 19 Hf and O "half-layers": here we define a full layer to consist of an Hf half-layer and an O half-layer) along the surface normal direction. Each half-layer consists of either two Hf or four O atoms, except for the outermost surface layers. The surface area of each side of the slabs corresponds to two bulk formula units. We constructed them initially from their relaxed bulk tetragonal and orthorhombic structures. The tetragonal slab has in-plane lattice vectors of 5.230×5.083 Å^2 or $c \times a\sqrt{2}$, where a and c are the lattice vector lengths of the tetragonal phase reported above. The corresponding vectors of the tetragonal slab with respect to the bulk are, namely, $\hat{a}$(slab) = $\hat{c}$(bulk), $\hat{b}$(slab) = $\hat{a}$(bulk)$-\hat{b}$(bulk), and $\hat{c}$(slab) is parallel to

$\hat{a}$(bulk)+$\hat{b}$(bulk), with the bulk tetragonal vectors defined above. The orthorhombic slab has in-plane lattice vectors of 5.056 × 5.274 Å^2 or $b \times a$, where b and a are the lattice vector lengths of the orthorhombic phase reported above. The corresponding vectors of the orthorhombic slab with respect to the bulk are, namely, $\hat{a}$(slab) = $\hat{b}$(bulk), $\hat{b}$(slab) = $-\hat{a}$(bulk), and $\hat{c}$(slab) is parallel to $\hat{c}$(bulk), with the bulk orthorhombic vectors defined above. We introduced a vacuum width of ~15 Å along the surface normal direction. We used a 4×4×1 *k*-point mesh for the supercell slabs. We allowed all atoms to relax until the absolute atomic force components were less than 0.01 eV/Å.

We fixed the middle five half-layers (three Hf and two O half-layers) during relaxation of the supercell slabs to simulate a bulk-like interior boundary condition for the surfaces. We introduced dipole corrections (both energy and potential) for the slabs constructed from the bulk orthorhombic phase to further eliminate spurious interactions between periodic images across the vacuum layer. **Table S3** shows calculations of the surface vibrational mode frequencies for the three lowest-energy surface compositions of the tetragonal and orthorhombic slab surfaces and confirms the ionically converged structures to be energy minima with no imaginary frequencies persisting along the relaxed coordinates [42].

To verify that the orthorhombic phase in the polar HfO_2 slabs persists towards the surface beyond the fixed middle layers, we plot in **Figure S4** the interlayer distances between each Hf half-layer to the next and the intralayer polar displacements of O atoms within each O half-layer for select stable surface compositions (vide infra) [42]. The spacings remain close to the bulk orthorhombic values except for the surface layers (which would be expected to deviate due to the presence of vacuum), validating the boundary condition choice we imposed.

D. Surface energy

To compare the thermodynamic stability of various surfaces, we evaluated their surface energy (γ). Following the derivation for a transition metal oxide discussed in prior bodies of work, see ref. [54], we first defined an average surface free energy (top and bottom surfaces) using the Gibbs free energy of a slab, $G^{slab}\left(T, p, N_{Hf}, N_O\right)$:

$$\gamma_{average} = \frac{1}{2A}\left(G^{slab}\left(T, p, N_{Hf}, N_O\right) - N_{Hf}\mu_{Hf}(T, p) - \; N_O\mu_O(T, p)\right) \tag{1}$$

where N_{Hf} and N_O are the numbers of Hf and O atoms in the slab supercell, μ_{Hf} and μ_O are the chemical potentials of Hf and O atoms in the reservoir (environment), and A is the surface area of one side of the slab. Because the bulk phase must be in equilibrium with the chemical reservoirs in order to exist, the Gibbs free energy of bulk HfO_2 must be: $g^{bulk}_{HfO_2}(T, p) \; = \; \mu_{Hf}(T, p) + 2\mu_O(T, p)$. Substituting $g^{bulk}_{HfO_2}(T, p) - 2\mu_O(T, p)$ for $\mu_{Hf}(T, p)$ in the $\gamma_{average}$ expression above, we have a surface energy expression that depends only on the chemical potential of O:

$$\gamma_{average} = \frac{1}{2A}\left(G^{slab}\left(T, p, N_{Hf}, N_O\right) - N_{Hf}g^{bulk}_{HfO_2}(T, p) - \left(N_O - 2N_{Hf}\right)\mu_O(T, p)\right) \tag{2}$$

We approximate the free energies of the bulk and the slabs using only DFT-PBE energies. This is because we expect that the vibrational free energy contributions from the bulk and surface mostly to cancel out. The chemical potential of oxygen, $\mu_O(T, p)$, can be expressed by the following Gibbs-Duhem equation for an ideal gas:

$$\mu_O(T, p) = \frac{1}{2}\mu_{O_2}(T, p) = \frac{1}{2}\mu_{O_2}(T, p^\circ) + \; \frac{1}{2}kTln\left(\frac{p}{p^\circ}\right) \tag{3}$$

where μ_{O_2} is the chemical potential of the O_2 gas and we need to find the temperature dependence of $\mu_O(T, p)$ at a particular partial pressure of O_2 (p, with $p° = 1$ bar). In this case, we chose the reference state of $\mu_O(T, p°)$ with respect to an isolated (gaseous) O_2 molecule:

$$\mu_O(T, p°) = \frac{1}{2}\mu_{O_2}(T, p) = \frac{1}{2}[\{H(T, p°, O_2) - H(0\ K, p°, O_2)\} - TS(T, p°, O_2)] \tag{4}$$

We express $H(0\ K, p°, O_2)$ as:

$$H(0\ K, p°, O_2) = 2\left(E_{\mathrm{O}}^{\mathrm{DFT}} - \Delta E_{f,O}(0\ K, p°)\right) \tag{5}$$

where $E_{\mathrm{O}}^{\mathrm{DFT}}$ and $\Delta E_{f,\mathrm{O}}(0\ \mathrm{K}, p°)$ are respectively the DFT energy of an O atom in vacuum (in a periodic asymmetric $8.0 \times 7.5 \times 7.0$ Å^3 box to obtain the ^{3}P ground state) and the empirically extrapolated formation energy of an O atom from O_2 at 0 K and 1 bar. The DFT-PBE binding error for O_2 can be as large as ~ 0.9 eV/O_2 [39], therefore requiring an empirical correction to the simulation of an isolated O atom in DFT instead. To calculate $H(T, p°, O_2) - H(0\ \mathrm{K}, p°, O_2)$, we first use the tabulated data for the reference enthalpy of O_2 at 1 bar for 0 K and 298 K to obtain $H(298\ \mathrm{K}, p°, O_2) - H(0\ \mathrm{K}, p°, O_2)$ [55], and then used the Shomate equation to determine the enthalpy at T relative to 298 K:

$$H(T, p°, O_2) - H(298\ \mathrm{K}, p°, O_2) = AT + {BT^2}/{2} + {CT^3}/{3} + {DT^4}/{4} - {E}/{T} + F - H \tag{6}$$

where **Table S4** displays the constants A to H for 100 - 700 K and 700 - 1000 K (taken from Ref. [56]). Hence:

$$\begin{aligned} &H(T, p°, O_2) - H(0\ \mathrm{K}, p°, O_2) \\ &\qquad = [H(T, p°, O_2) - H(298\ \mathrm{K}, p°, O_2)] + [H(298\ \mathrm{K}, p°, O_2) - H(0\ \mathrm{K}, p°, O_2)] \end{aligned} \tag{7}$$

Similarly, for $S(T, p°, O_2)$ we used the Shomate equation:

$$S(T, p°, O_2) = A \ln T + BT + {CT^2}/{2} + {DT^3}/{3} - {E}/{2T^2} + G \tag{8}$$

using the same above-mentioned constants and an additional constant G (also shown in **Table S4**) [42].

III. Results and Discussion

A. Bulk Structures

We used the conventional two-formula-unit structure shown in **Figure 1(a)** for the initial bulk structure convergence of the tetragonal (*$P4_2/nmc$*) phase. The orthorhombic (*$Pca2_1$*) HfO_2 unit cell can be regarded as a distorted tetragonal HfO_2 unit cell where half the unit resembles, with minor distortion, the parent tetragonal phase while the other half exhibits significant polar distortions [6,57]. Reorientation of the tetragonal phase (**Figure 1(b)**) such that planes that consist exclusively of Hf and O atoms align with the analogous planes in the orthorhombic phase (**Figure 1(c)**), which better illustrate the transformation from the nonpolar tetragonal to the polar orthorhombic HfO_2 phase. The polarization along the [001] axis of the orthorhombic phase corresponds to the polarization along the [110] axis of the tetragonal phase accompanying the changes in the length of the lattice vectors (compare **Figure 1(b)** and **Figure 1(c)**). The bulk atomic structures (and the surfaces in the following sections) were visualized using VESTA [58].

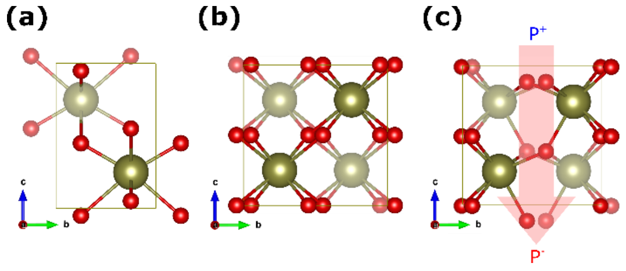

Figure 1: (a) Structure of the conventional two-formula-unit nonpolar tetragonal ($P4_2/nmc$) HfO_2 phase. (b) Four-formula-unit supercell of the tetragonal phase shown in (a), re-oriented such that the new *a*, *b*, and *c* axes are now along $[\bar{1}10]$, [001], and [110] directions of the conventional tetragonal vectors, respectively. (c) Four-formula-unit supercell of the polar orthorhombic ($Pca2_1$) HfO_2 phase. The polarization vector lies along the *c*-axis [001] direction, as indicated by the overlaid arrow. For all the structures, Hf and O atoms are shown as green (large) and red (small) spheres, respectively. The fainter atoms are farther away from the viewer.

B. Surface Structures

We constructed supercell slab structures consisting of nine Hf and ten O half-layers (~ nine-formula-units thick with each half-layer composed of either two Hf or four O atoms, i.e., two-formula units) from their respective nonpolar bulk tetragonal ((110) surface) and polar bulk orthorhombic ((001) surface) phases such that the polarization vector points normal to the surface of the orthorhombic slab (as portrayed in **Figure 1**, see also Methods section for a more detailed description on how the slabs were constructed). Additionally, we fixed the middle three Hf and two O half-layers for all slabs to their bulk-like arrangement to simulate a semi-infinite-bulk-like boundary condition for the surface atoms and to avoid spurious phase transformations.

We then generated slab supercells with surfaces of varying composition terminated with the following stoichiometric or off-stoichiometric terminations per surface unit cell: 2.0-O, 1.5-O, 1.0-O, 0.5-O, 1.0-Hf, and 0.5-Hf. We named the surfaces according to the atoms that compose their outermost layer and their number per formula unit. Each surface unit cell has an area corresponding to two-formula units (see **Figures 2** and **3** and their corresponding legend), therefore, an O-terminated surface with three O atoms per surface unit cell is named 3/2-O or 1.5-O, so that the names reflect the surface composition per surface formula unit. Among the compositions explored, the stoichiometric slabs are those with 1.0-O or 0.5-Hf terminations on both surfaces. We created the surfaces by removing O or Hf atoms starting from slabs with either 2.0-O or 1.0-Hf surfaces until we achieved the compositions listed above. We included slab supercells consisting of both compositionally symmetric and asymmetric surface terminations to explore the effect of the positive versus negative surface polarizations of the polar slabs in stabilizing different surface compositions. Therefore, along with compositionally symmetric slabs, namely, 2.0-O/2.0-O, 1.5-O/1.5-O, 1.0-O/1.0-O, 0.5-O/0.5-O, 1.0-Hf/1.0-Hf, and 0.5-Hf/0.5-Hf, we studied a select set of compositionally asymmetric slabs, namely, 1.5-O/1.0-O, 1.5-O/0.5-O, and 1.5-O/0.5-Hf (we provide below a rationale on why we targeted these asymmetric slabs). We named the slabs according to the composition of their top and bottom surfaces (whose naming scheme is discussed above). For example, 1.0-O/1.0-O refers to a supercell slab with both top and bottom surfaces terminated with two O atoms per surface unit cell (recall a surface unit cell is composed of two formula units, therefore the designation 1.0-O shows surface composition in per surface formula unit basis as explained above). Surface 1.5-O/1.0-O refers to a supercell slab with three O atoms per surface unit cell at one surface and two O atoms per surface unit cell at the opposite surface. Note that for the orthorhombic slab, the top surface faces the positive polarization, while the bottom surface faces the negative polarization.

It is possible to construct several unique permutations of the same surface composition when starting with an unrelaxed slab constructed from atomic positions in the respective bulk phase of the tetragonal and orthorhombic HfO_2 crystals. The initial surface configuration influences the surface energetics and not all supercell slabs necessarily relax to the same final structure or energy.

For example, for a supercell slab constructed from the bulk orthorhombic phase, we can create a single O vacancy by removing an O from either the polar or nonpolar half-unit (see **Figure 1(c)**c). The data and structures presented here are calculated for the most thermodynamically stable of the multiple unique initial surface configurations explored. We explored other surface configurations of the same surface type; **Tables S5** and **S6** provide a tabulation of the number of configurations sampled and their average surface energies at 900 K and 1 bar O_2 [42]. For some surface compositions, the surface energy is very dependent on the initial unrelaxed surface construction, e.g., for the orthorhombic 1.0-O/1.0-O slabs, surface energies varied by a range of 0.55 J/m^2 (**Table S6**) [42].

Figures 2 and **3** respectively show the surface views of the relaxed nonpolar and polar slabs for the range of surface compositions explored. We faded-out the atoms lying in deeper layers in the surface view for clarity and the atoms in the outermost layers within a 1×1 unit cell area are circled. Additionally, the full profile view shows the most stable compositionally symmetric and asymmetric slabs.

For the polar orthorhombic slabs, we later discuss the need for construction of asymmetric surface terminations shown in **Figure 3(b)** to identify the thermodynamically most stable ferroelectric surfaces. For direct comparison to these asymmetric surface compositions, we also construct nonpolar tetragonal slabs shown in **Figure 2(b)** that parallel the asymmetric surface compositions of the polar orthorhombic slabs.

The reconstructions after relaxation of both surfaces of the compositionally symmetric nonpolar slabs mirror each other, as expected. The reconstructions of the two surfaces of the compositionally asymmetric nonpolar slabs, on the other hand, do not lead to the same structural configuration as the surfaces from their equivalent compositionally symmetric slab counterpart.

For the polar slabs, two surfaces with a symmetric composition but with opposite polarization, positive (P+) for the top and negative (P-) for the bottom, did not reconstruct to be mirror configurations after relaxation. In almost all cases, the surface atoms roughly remain in their bulk-like lattice positions in the surface plane with primary relaxations along the surface normal – this is true for both the tetragonal and orthorhombic phases (**Figures 2** and **3**). The only glaring exception is the 1.5-O/1.5-O orthorhombic slab where the P- O atoms undergo significant rearrangement, which will we discuss in more detail below.

In the following sections, we discuss the relative stabilities of the surface structures and evaluate their electronic structures as a means to explain their stability or instability. We proceed with the nonpolar cases first; then we compare them with the polar cases.

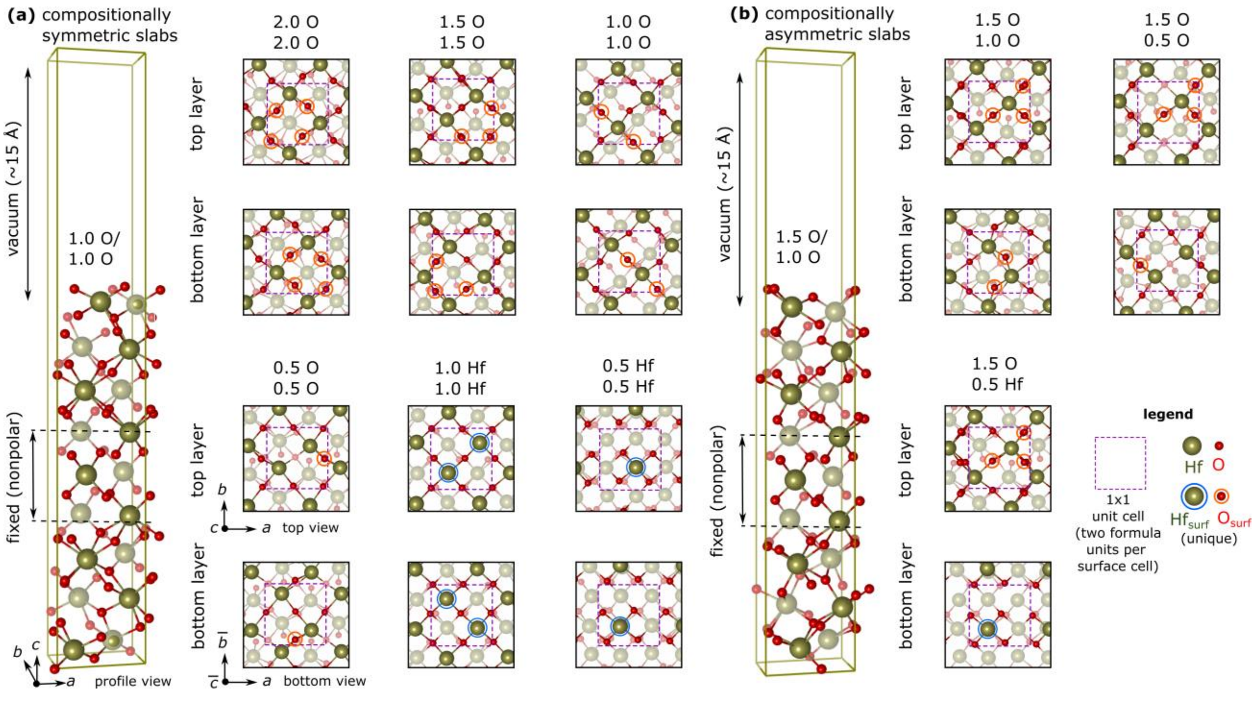

Figure 2: Relaxed structures for compositionally (a) symmetric and (b) asymmetric nonpolar tetragonal HfO_2 supercell slabs. Profile views are shown only for the most stable compositionally symmetric and asymmetric slabs among all compositions studied. Top and bottom views of the

slabs are shown for the most stable configuration for a given composition. The composition of the outermost layers in terms of atoms per surface unit cell is labeled for the top and bottom layer above each structure. The fainter atoms are farther away from the viewer. Outermost atoms are circled within a 1x1 lateral unit cell that contains two formula-units (purple-dashed box).

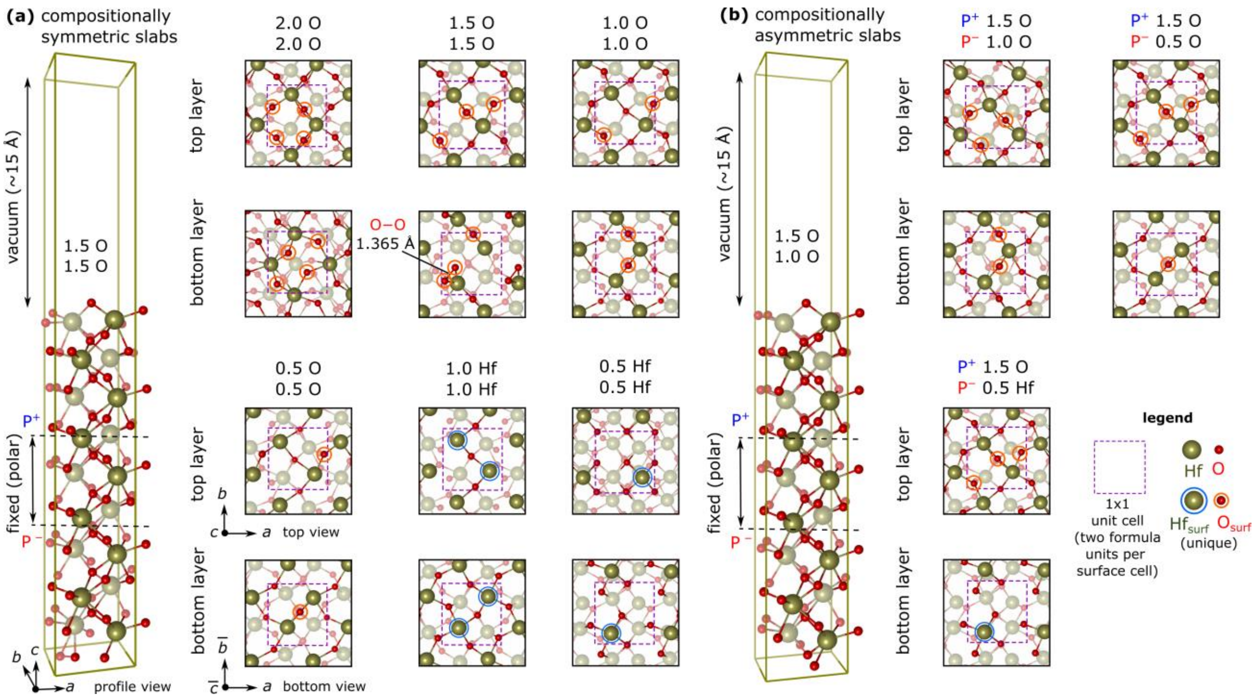

Figure 3: Relaxed structures for most stable compositionally (a) symmetric and (b) asymmetric orthorhombic HfO_2 supercell slabs. Profile views are shown only for the most stable compositionally symmetric and asymmetric slabs among all compositions studied. Top and bottom views of the slabs are shown for the most stable configuration for a given composition. The composition of the outermost layers in terms of atoms per surface unit cell is labeled for the top (P+) and bottom (P-) layer above each structure. To disambiguate the nomenclature for the compositionally asymmetric slabs, we use P+ and P- to refer to the composition of the positively and negatively polarized surfaces, respectively. The fainter atoms are farther away from the viewer. Outermost atoms are circled within a 1x1 lateral unit cell that contains two formula-units (purple-dashed box).

C. Surface Energies

Figures 4 and **5** display the surface energies for the most thermodynamically stable configurations of tetragonal HfO_2(110) and orthorhombic HfO_2(001) slabs at each surface composition explored as a function of both temperature (at 1 bar O_2) and pressure (at 900 K). Experimentally relevant ranges for crystallization of HfO_2 thin films were used for the choice of temperature and pressure: magnitudes of pressure experimentally explored range from ultra-high vacuum to high pressure annealing and temperatures up to near 1100 K have been applied to explore the tetragonal/orthorhombic phase boundary [21,59-61].

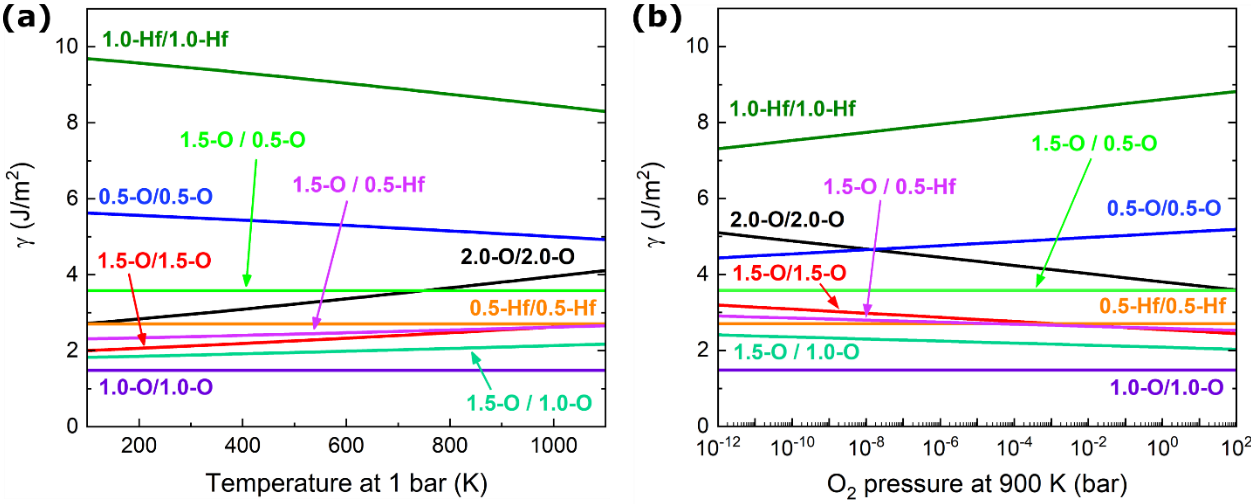

Figure 4: Plot of surface energy as a function of (a) temperature from 100 K to 1100 K and (b) pressure from 10^{-12} bar to 10^{2} bar for compositionally symmetric and asymmetric tetragonal HfO_2(110) slabs.

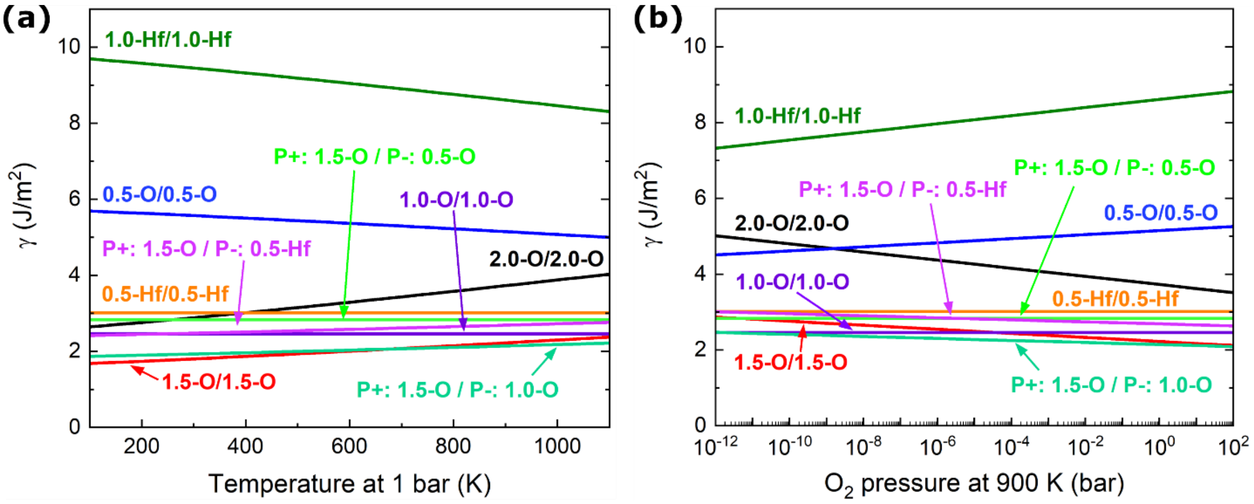

Figure 5: Plot of surface energy as a function of (a) temperature from 100 K to 1100 K and (b) pressure from 10^{-12} bar to 10^{2} bar for compositionally symmetric and asymmetric orthorhombic $HfO_2(001)$ slabs. To disambiguate the nomenclature for the compositionally asymmetric slabs, we use P+ and P- to refer to the composition of the positively and negatively polarized surfaces, respectively.

The slope of the surface energies arises from off-stoichiometry from the bulk Hf:O ratio of 1:2, which is reflected in the term $(N_O - 2N_{Hf})\mu_O(T,p)$ in the reduced surface energy expression (section II-D). When $N_O > 2N_{Hf}$, then the average surface energy ($\gamma_{average}$) positively correlates with $\mu_O(T,p)$ whereas when $N_O < 2N_{Hf}$, a negative correlation between $\gamma_{average}$ and $\mu_O(T,p)$ exists. On the other hand, $\mu_O(T,p)$ of the reservoir decreases with temperature T (primarily due to an increase in gas-phase entropy) but increases with O_2 partial pressure p (as expressed in the Gibbs-Duhem relation for an ideal gas, section II-D). The former (off-stoichiometry) factor explains the varying dependence of surface energies with T and p among different compositions, while the latter (chemical potential) factor explains the opposite T and p trend for a given composition in **Figures 4** and **5**.

For the compositionally symmetric tetragonal slabs (i.e., ignoring 1.5-O/1.0-O, 1.5-O/0.5-Hf, and 1.5-O/0.5-O), the relative ordering of the surfaces with respect to stability for $100 < T \leq 1100$ K and 1 bar **Figure 4(a)**) is: 1.0-O > 1.5-O > 0.5-Hf > 2.0-O > 0.5-O > 1.0-Hf, where ">" means more stable. Comparing to the compositionally symmetric ferroelectric orthorhombic slabs (**Figure 5(a)**), the same relative ordering of the surface stability holds at 400 - 1100 K and 1 bar except 1.5-O > 1.0-O (i.e., the 1.5-O/1.5-O line is lower in energy than the 1.0-O/1.0-O line within the entire temperature range investigated in **Figure 5(a)**). The relative stability of 0.5-Hf and 2.0-O switches to 2.0-O > 0.5-Hf for $T < 400$ K (i.e., the 0.5-Hf/0.5-Hf line is higher in energy than the 2.0-O/2.0-O line at lower temperatures). We discuss later the effect of having asymmetric stoichiometries between the top and bottom terminations on the surface energies.

We can interpret the trends in stability of the surfaces primarily through electrostatics (in the absence of strong quantum mechanical influence, e.g., the breaking of covalent bonds producing “dangling bonds”). In general, a nonpolar surface is electrostatically stable without further surface modification or reconstruction needed (atomic or electronic). If one considers the tetragonal slab to be constructed from perfectly ionic equally spaced layers of pure Hf^{4+} and O^{2-} building blocks, one should expect from simple charge accounting that the compositionally symmetric slabs that exhibit bulk stoichiometry (Hf:O = 1:2), namely, 1.0-O/1.0-O and 0.5-Hf/0.5-Hf slabs to be stable [62]. Indeed, the stoichiometric slab with a symmetric 1.0-O/1.0-O surface composition is lowest in energy (**Figure 4**). We can attribute the higher instability of the compositionally symmetric 0.5-Hf/0.5-Hf terminated surface to the more significant loss in the coordination number (higher number of dangling bonds) of Hf compared to O at the surface compared to the bulk. Deviation from either of the above-mentioned compositions leads to higher energy. An excess of O is less destabilizing than a deficiency of O: compare 1.5-O/1.5-O and 0.5-O/0.5-O in **Figure 4**. As expected, the former oxidizes surface O species while the latter reduces the Hf atoms in the layers below (*vide infra*). 1.0-Hf/1.0-Hf is very unstable (**Figure 4**) due to the surface Hf^{4+} being reduced to lower oxidation states and a higher number of Hf dangling bonds.

Next, we consider stability trends for the polar orthorhombic slabs compared to the nonpolar tetragonal slabs. Despite similar composition between the tetragonal and orthorhombic phases, the non-centrosymmetric displacements of the Hf and O planes along the [110] direction of the tetragonal phase, which is along the [001] direction of the orthorhombic phase, result in a dipole and thus a polar (001) surface of the orthorhombic phase. We expect a polar surface to be compensated by a surface charging mechanism which generally occurs through a modification of the number surface ions to form nonstoichiometric surfaces or through electronic reorganization and electron transfer towards or away from the surface, producing, e.g., surface metallization. We understand the former to be preferential as the compensation mechanism [35,36,63-65], given an available chemical reservoir that can exchange with ions or molecules. Here, the formation of polar orthorhombic slab surfaces resulting in a nonstoichiometric deviation from the bulk indeed leads to some degree of stabilization for the polar orthorhombic slab surfaces: compare 1.5-O/1.5-O vs 1.0-O/1.0-O in **Figure 5**. Despite the compositional symmetry of the surfaces in 1.5-O/1.5-O, the distinct ability of O to form a bond with another surface O leads to formally compositionally asymmetric P+ and P- surfaces. As **Figure 3a** shows, the 1.0-O/1.0-O has all of its surface O coordinated only with Hf on both terminations – this in fact leads to surface metallization to (partly) screen the surface polarization (*vide infra*). In the 1.5-O/1.5-O, on the other hand, a pair of surface O on the P- surface form a bond of length 1.37 Å (**Figure 3a**), reminiscent of an average between a peroxide and superoxide bond [66]. This rearrangement does not appear in the corresponding 1.5-O/1.5-O tetragonal slab (**Figure 2(a)**). The formation of an O−O bond is favored on the P- because this surface would otherwise favor p-doping (O_2^{n-} species are an oxidized form of O^{2-} which may act as a positive localized surface defect). This eliminates the need for the P- to metallize (p-doped) to screen the polarization charge (*vide infra*).

In fact, we can construct an orthorhombic slab with asymmetric composition between surfaces that has an even lower average surface energy which requires only half an additional O per surface-formula-unit at the P+ surface (to disambiguate the nomenclature for the compositionally asymmetric slabs, we use P+ and P- to refer to the composition of the positively and negatively polarized surfaces, respectively). For example, at 900 K and 1 bar, this asymmetric orthorhombic slab with a surface composition of P+:1.5-O/P-:1.0-O has an average surface energy of 2.14 J/m^2 compared to 2.22 J/m^2 for the compositionally symmetric case of 1.5-O/1.5-O (**Figure 5**). Although asymmetric reconstruction appears to be an effective mechanism to stabilize the polar phase, other examples of such modifications, namely, P+:1.5-O/P-:0.5-O and P+:1.5-O/P-:0.5-Hf, do not improve the average surface energy. The two latter examples expose more undercoordinated Hf, which also is unfavorable for the tetragonal phase. In P+:1.5-O/P-:0.5-O, the removal of O from, e.g., P-:1.0-O or P-:1.5-O to yield P-:0.5-O composition exposes the Hf in the layer below (**Figure 3**).

The tetragonal slabs with an asymmetric surface termination have surface energies that are almost the average of energies of the surface stoichiometries from which they are derived. For example, the surface energy at 900 K and 1 bar is 2.09 J/m^2 for the 1.5-O/1.0-O slab, which is roughly the average of 2.53 J/m^2 and 1.49 J/m^2 that correspond to the surface energies of the 1.5-O/1.5-O and 1.0-O/1.0-O slabs (**Table S5**) [42]. In contrast, the average surface energy of P+:1.5-O/P-:1.0-O (2.14 J/m^2) is lower than that of the average (2.34 J/m^2) of the surface energies of the orthorhombic slabs 1.5-O/1.5-O (2.22 J/m^2) and of 1.0-O/1.0-O (2.46 J/m^2) at the same temperature and pressure (**Table S6**) [42].

D. Surface Bader Charges

To obtain further insight into the electronic charge redistribution that leads to stabilization of the polar orthorhombic HfO_2 slabs with 1.5-O/1.5-O and P+:1.5-O/P-:1.0-O surface terminations over the 1.0-O/1.0-O surface termination, we calculated the Bader charges of O and Hf in each layer. The Bader charge analysis [67,68] partitions the continuous charge density into atomic charges and because HfO_2 is largely ionic, this analysis is an appropriate choice to assign atomic charges. **Figure 6** displays the charge deviation layer-by-layer in both tetragonal and orthorhombic slabs, where we see the major changes occur near the surface, induced by the ferroelectric polarization in the middle bulk layers in the orthorhombic slab. We calculated the deviation of the charge per atom within the slab with respect to the average Bader charge values of Hf and O in their respective bulk phases (tetragonal or orthorhombic). The calculated Bader charges in the tetragonal phase are 9.41 *e* for Hf and 7.30 *e* for O (corresponding to the outer core/valence electrons only, i.e., not including the electrons subsumed into the PAW potentials), and in the orthorhombic phase are 9.41 *e* for Hf and 7.31 *e* and 7.29 *e* for the two types of O. In comparison, the valence charges should be 12 *e* ($5s^2 5p^6 6s^2 5d^2$) for neutral Hf and 6 *e* ($2s^2 2p^4$) for neutral O. In the orthorhombic phase, the O takes two values that differ by 0.02 *e* depending on their location in the polar or nonpolar half-unit.

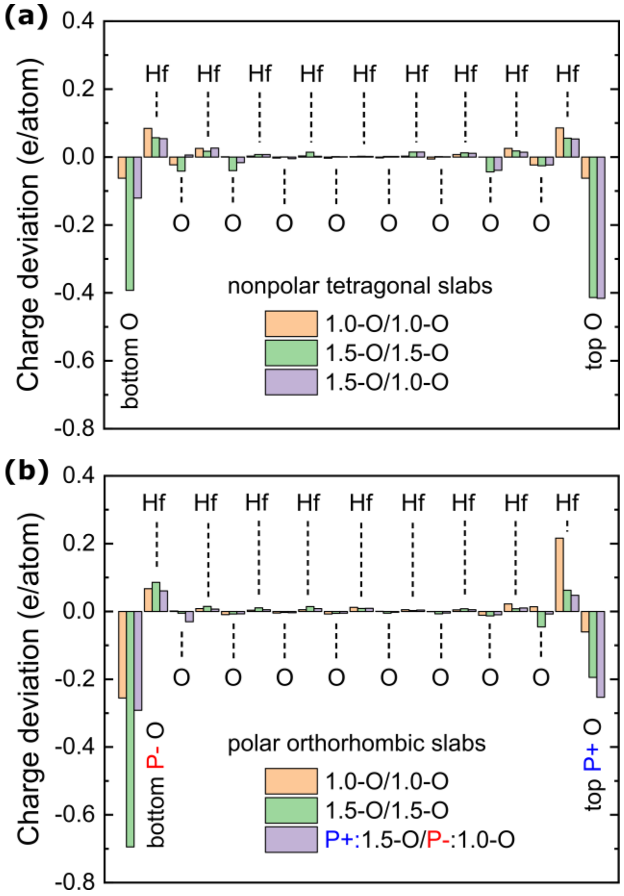

Figure 6: Layer-by-layer Bader charge deviation for (a) nonpolar tetragonal and (b) polar orthorhombic HfO_2 slabs for three different compositions. The values correspond to the average Bader charge deviation per atom for each Hf and O half-layer relative to their respective bulk phase. Note that the left- and right-hand sides of the plots correspond respectively to the bottom and the top of the slabs. In the surface nomenclature, the composition of the top surface is given first. Figures 2 and 3 show the corresponding atomic structures of the compositions indicated.

The tetragonal HfO_2 with a symmetric 1.0-O/1.0-O surface composition yields Bader charges of O at the surface closest to the bulk value, which indicates that they are fully ionized to a bulk-like oxidation state (**Figure 6a**). The symmetric cases (1.0-O/1.0-O and 1.5-O/1.5-O) have symmetric distributions of charge across the slabs, as expected. In the tetragonal cases with excess O, i.e., 1.5-O/1.5-O and 1.5-O/1.0-O, the surface O atoms on the 1.5-O surface contain fewer electrons (negative change deviation, oxidized) with some additional depletion of O charge (although significantly less) within the inner layers across the slab (**Figure 6a**). For the asymmetric 1.5-O/1.0-O termination, the charge deficiency of the O atoms is asymmetric, where the 1.5-O surface corresponds to the 1.5-O surface in the symmetric 1.5-O/1.5-O slab (0.41 *e*/atom and 0.42 *e*/atom, respectively), and the 1.0-O surface has a charge deficiency of 0.12 *e*/atom which lies closer to the value of 0.06 *e*/atom in the symmetric 1.0-O/1.0-O slab.

In compositionally symmetric orthorhombic slabs, we expected electrons to transfer from the P- to the P+ surface as a screening mechanism in order to eliminate the polarization field. Comparing the most thermodynamically stable nonpolar tetragonal 1.0-O/1.0-O slab to its ferroelectrically polarized counterpart in the orthorhombic 1.0-O/1.0-O slab, an additional deficiency of -0.19 *e*/atom exists at the P- surface. At the positive P+ surface, the charge deficiency (0.06 *e*/atom) equals to that of the tetragonal phase, instead, the excess electron (0.28 *e*/atom) accumulates in the Hf half-layer below (**Figure 6b**).

The addition of an O to both surface unit cells of the orthorhombic 1.0-O/1.0-O slab to arrive at the more thermodynamically stable orthorhombic 1.5-O/1.5-O slab shows that the excess accumulation of electrons decreases at the P+ surface (**Figure 6b**). This indicates that the addition of O can adequately provide the ionic charge to screen the ferroelectric polarization with a smaller need for electronic charge redistribution across the slab (the excess O on the 1.5-O P+ surface also ionizes more than in the tetragonal phase). However, a large excess of O on the P- surface that is already electron-deficient yields even more electron-deficient surface O atoms (associated with the emergence of the surface O_2^{n-} species, *vide supra*), decreasing by approximately 0.44 *e*/atom. This indicates that while the addition of O on the P+ surface is favorable, it leads to the destabilization of the P- surface. The removal of an O from the P- surface of the 1.5-O/1.5-O slab to yield the P+:1.5-O/P-:1.0-O slab alleviates this electron deficiency and thus can explain further stabilization of the asymmetric slab compared to the symmetric 1.5-O/1.5-O (**Figure 5**).

The charge deviation for the nonpolar and polar slabs relative to their respective bulk phases in **Figure 6** is partially a result of the charge redistribution from the cleaved bonds at the surface and for some (1.5-O/1.5-O and 1.5-O/1.0-O) due to off-stoichiometry. To isolate and quantify the charge redistribution that occurs in the polar slabs to screen the ferroelectric polarization in the bulk-like middle layers, we plot in **Fig. S5** the layer-by-layer Bader charge difference between the polar orthorhombic slabs and nonpolar tetragonal slabs of the same compositions shown in **Figure 6** [42]. For the symmetric 1.0-O/1.0-O polar slab, this difference is 0.16 *e*/atom (excess electron) for the Hf and O sub-layers at the P+ surface. A complementary deviation of -0.20 *e*/atom (electron deficiency) is calculated for the outermost O half-layer at the P- surface. These calculated charge deviations are consistent with the analysis in Figure 6b, in that charge carriers of the opposite charge to the polarization charge are expected (and observed) to migrate to screen the latter. Note that the polar slabs with symmetric 1.5-O/1.5-O and asymmetric P+:1.5-O/P-:1.0-O compositions also have excess and deficiency of electrons at the P+ and P- surfaces, respectively, as expected. In fact, the net charge redistribution based on **Fig. S5** appears to be nearly independent of the composition [42]. The difference arises only as to where the excess electron resides on the P+ side. While Fig. 6b shows that for 1.5-O/1.5-O and P+:1.5-O/P-:1.0-O, the outermost O atoms are not fully ionized relative to the bulk, **Fig. S5** shows they are more ionized on the P+ surface of the orthorhombic slab than on the non-polar tetragonal slab [42]. Of note, the negative screening charge on the P+ surface can be clearly ascribed to the excess O atoms on the 1.5-O surfaces (therefore, ionic in nature), whereas for the 1.0-O surface, the excess electron on the Hf sub-layer screens the P+ charge. In all cases, on the P- surface, the screening is due to electron deficiency on the outermost O half-layer. The exact contribution from ionic charge cannot be fully quantified because the degree to which the adsorbates are ionized on the surface depends on both the overall stoichiometry of the slab and the ferroelectric polarization strength. Further illumination on the nature of polarization charge screening follows.

E. Rationalizing stability via electrostatic potential and projected DOS

To study the electronic response of ferroelectric HfO_2 to the built-in electric field, we calculated and plotted the plane(*xy*)-averaged electrostatic potential (blue lines) and its out-of-plane running average ("z-averaged", within 5.09 Å windows, red lines) along the direction normal to the slab (**Figure 7**). The flat electrostatic potential in the vacuum on each side of the slabs confirms that the vacuum thickness is large enough and that the dipole correction is effective in removing spurious interaction between slabs. The nonpolar 1.0-O/1.0-O tetragonal slab displays a symmetric profile across both surfaces from the center of the slab (**Figure 7a**). In contrast, for the polar 1.0-O/1.0-O slab, the ionic displacement associated with the tetragonal to orthorhombic HfO_2 phase transition in the bulk layers sets up a potential gradient across the slab (**Figure 7b**). As a result, a difference remains in the work function between the P+ surface and P- surface of -4.25 eV. From the slope of the *z*-averaged electrostatic potential across the fixed middle layers of the slab, we approximate the electric field to be roughly -0.34 V/Å. This electric field drives the accumulation of excess charge observed in the Hf half-layer on the P+ surface (**Figure 6b**). We examine below how this large electrostatic potential leads to the dielectric breakdown, as visualized in **Figure 8**.

The addition of O to both surfaces in the case of the polar 1.5-O/1.5-O slab (**Figure 7c**) serves to reduce the electrostatic potential difference, and we observe a reduction in the magnitude of the difference in the work function between the two surfaces and the electric field to 0.7 eV and 0.186

V/Å, respectively. Removal of an O from the P- surface of the 1.5-O/1.5-O slab to yield the P+:1.5-O/P-:1.0-O slab (**Figure 7d**) alleviates the deeper potential on the P- surface and causes the slope of the electrostatic potential to vanish – the magnitude of the difference in the work function and the electric field decreases to -0.07 eV and 0.03 V/Å, respectively.

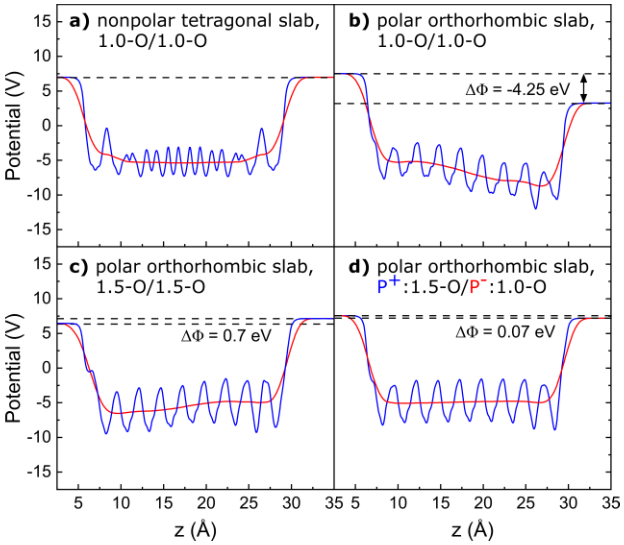

Figure 7: Plane-averaged electrostatic potential comprised of the ionic and Hartree potentials (blue) and the *z*-averaged (5.09 Å window) potential (red), calculated along the surface normal for the tetragonal(110) surface with (a) symmetric 1.0-O/1.0-O composition and orthorhombic(001) surfaces with (b) symmetric 1.0-O/1.0-O, (c) symmetric 1.5-O/1.5-O, and (d) asymmetric P+:1.5-O/P-:1.0-O compositions. The potentials are referenced to the Fermi level. The horizontal dashed lines mark the positions of the vacuum level for each surface. The difference in the work functions (ΔΦ) is the difference in the vacuum potentials of the two surfaces multiplied by a unit of elementary charge *e* = 1. Note that the left- and right-hand sides of the plots respectively correspond to the bottom and the top of the slabs. In the surface nomenclature, the composition of the top surface is given first. For the corresponding structures, see Figures 2 and 3.

Figure 8(a) shows a layer-by-layer projected densities of states (pDOS) for the most stable tetragonal slab with symmetric composition of 1.0-O/1.0-O and **Figure 8(b)** shows its orthorhombic counterpart with the same symmetric composition. The top pDOS in each panel of **Figure 8** corresponds to the top (P+ for orthorhombic) surface O layer for each structure. Each subsequent pDOS going downward in each panel corresponds successively to the Hf or O half-layer below, with the lowest pDOS corresponding to the bottom (P- for orthorhombic) surface O layer. Note how the bands hardly shift relative to the band edges of the middle layers for the 1.0-O/1.0-O tetragonal slab, except for the outermost layers as expected due to the change in their coordination environments (**Figure 8(a)**). An increased density of O states exists at the surface, but the O atoms remain fully reduced and closed shell. The nonpolar tetragonal slab also remains insulating throughout the slab as in the bulk (see **Figure S3(a)** for the bulk tetragonal electronic DOS) [42].

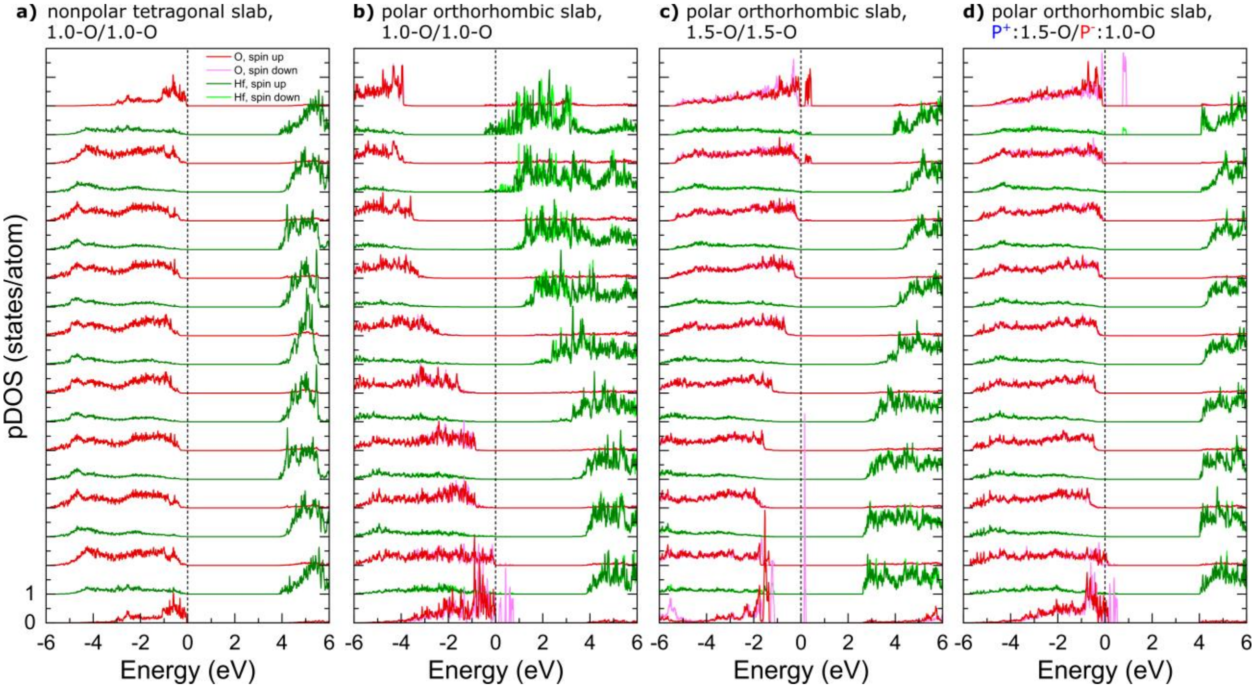

Figure 8: Layer-by-layer pDOS for the tetragonal HfO_2(110) surface with (a) symmetric 1.0-O/1.0-O composition and orthorhombic (001) surfaces with (b) symmetric 1.0-O/1.0-O, (c) symmetric 1.5-O/1.5-O, and (d) asymmetric P+:1.5-O/P-:1.0-O compositions. The electronic energies reference to the valence-band edge or the Fermi level (dashed vertical lines mark Energy = 0 eV). The top O layer of the polar orthorhombic slab corresponds to the P+ surface and the bottom O layer corresponds to the P- surface. Hf half-layer spin up/down: green/light green; O half-layer spin up/down: red/pink. The values are shifted so that the pDOS of the top and bottom layers correspond respectively to the top-most and bottom-most curves. Figures 2 and 3 show the corresponding atomic structures.

It is known that large electric fields originating from the spontaneous polarization of ferroelectrics induce band bending at ferroelectric surfaces and interfaces [64,69-72]. The net macroscopic field from the steep electrostatic field (**Figure 7b**) dramatically shifts the bands as a function of position across the slab in the polar orthorhombic slab (compare **Figures 8a** and **8b)**. Examining the pDOS starting at the top surface (P+) of the orthorhombic slab (**Figure 8b**), we see that the Fermi level is now above the conduction band edge of the outermost Hf sublayer, indicating that the interface is conducting (n-doped). Moving towards the bulk, the conduction and valence bands both rise in energy almost linearly, such that the Fermi level lies roughly in the middle of the bulk frontier states. The increase in energy of the frontier states continue while descending down the slab layers, where finally at the bottom surface (P-), we see that the Fermi level now lies below the (O-derived) valence band edge, making that surface also conducting (p-doped). Additionally, spin polarization reveals induced magnetic moments for both the (reduced) Hf and (oxidized) O atoms near and at the surface of the orthorhombic slab.

Figures 8(c) and **8(d)** show the pDOS for the most thermodynamically stable compositionally symmetric (1.5-O/1.5-O) and asymmetric (P+:1.5-O/P-:1.0-O) orthorhombic slabs. In contrast to the 1.0-O/1.0-O orthorhombic slab in **Figure 8(b)**, the more stable 1.5-O/1.5-O orthorhombic slab in **Figure 8(c)** exhibits a reduction in band bending across the sublayers, which we attribute to the additional ionic charge that screens the macroscopic electrostatic potential from the ferroelectric polarization in the bulk. In general, the accumulation of excess charge as a charge screening mechanism that leads to the filling of the surface conduction bands in ferroelectric oxides is energetically expensive as the potential across the slab (prior to charge redistribution) would need to be greater or equal to the band gap, which for HfO_2 is at least ~4.34 eV (**Figure S3**, [42]) [65]. The emergence of nonstoichiometric polar HfO_2 slabs provides the additional ionic charge that can effectively screen ferroelectric polarization, avoiding the need for surface metallization as a charge screening mechanism.

The addition of O on the P+ surface of the 1.5-O/1.5-O orthorhombic slab eliminates the need to n-dope the top Hf sublayer (compare the topmost Hf layer pDOS in **Figure 8(c)** to **8(b)**). In **Figure 8(c)**, the Fermi level of the top surface (P+) now lies at the valence band edge, making the surface insulating, although localized empty states exist above the Fermi level in this layer (a complete reversal compared to the orthorhombic 1.0-O/1.0-O termination where the Hf sublayer of the P+ surface is n-doped, **Figure 8(b)**). Although an excess O on the P- surface is in principle electrostatically unfavorable, the emergence of O_2^{n-} on this surface of the 1.5-O/1.5-O orthorhombic slab (**Figure 3(a)**) provides a net positive defect (for $n < 2$, because it replaces an otherwise surface O^{2-} ion) that is favored on the P- surface. This mechanism in fact eliminates the metallization of the P- surface (compare the bottom O layer pDOS in **Figure 8(c)** to **8(b)**). However, at the P- surface, an O-derived state exists just above the Fermi level (**Figure 8(c)**, associated with the O_2^{n-} species). Spin polarization is also induced, especially for the P- surface O atoms (once again consistent with the O_2^{n-} species).

Finally, as previously highlighted, the most stable orthorhombic slab favors an asymmetric surface composition (P+:1.5-O/P-:1.0-O). Keeping the excess O on the P+ while removing it on the P- surface ultimately leads to enhanced stabilization and removal of band bending (**Figure 8(d)),** although the p-doped metallic character of the P- surface persists as in the orthorhombic 1.0-O/1.0-O case. The O atoms are fully ionized except for the outermost P+ and P- O atoms. The emergence of the empty gap states on the P+ surface indicate that more O is present than is needed to screen the positive polarization charge - a lower excess O coverage would suffice, although the limited simulation supercell size does not capture this effect.

The stability of asymmetric oxygen termination at the P+ and P- surfaces can partially explain the observed "wake-up effect" in HfO_2-based ferroelectrics that increases the orthorhombic/tetragonal phase fraction and stabilizes the strength of ferroelectric polarization after electric field cycling [27,34,73-76]. After crystallization of HfO_2 via a nonpolar tetragonal phase pathway, the instability of the stoichiometric surfaces (which the tetragonal nonpolar phase initially favors) would disfavor the persistence of polar ferroelectric grains after polarization with an electric field. In the context of these prior observations and proposed mechanisms of the wake-up effect, redistribution of O vacancies near the surfaces or interfaces of HfO_2 films through electric-field cycling then could contribute to the sustained stabilization of ferroelectric polarization after many cycles.

IV. Summary and outlook

We constructed nonpolar slabs from the bulk tetragonal HfO_2 phase composed of alternating pure Hf and pure O half-layers along the [110] direction. We found the most stable (110) surface to be O-terminated with only one O atom present per surface formula unit, instead of two O. The slab maintains overall stoichiometry and the stable reconstruction satisfies simple electrostatic requirements to eliminate electrostatic potential divergence when truncating along this direction where alternating positive (Hf) and negative (O) planes exist.

For the corresponding (001) surface in the structurally related ferroelectric orthorhombic phase, we found polarization to have a nontrivial influence on the surface energetics. Surface-polarization charge, due to the bound charge displacements within the slab, favors a deviation in the surface composition relative to the nonpolar surface. Specifically, the positively polarized surface remains O-terminated but favors a composition with 1.5 O per surface formula unit, while the negatively polarized surface still favors one O per surface formula unit.

The ferroelectric polarization induces an increase in the electrostatic potential across the slab that leads to band bending (as illustrated in layer-by-layer pDOS) and is associated with an unstable surface configuration in slabs whose only means of polarization screening occurs through a major charge redistribution and electronic reorganization that metallizes the surface. Thus, ionic passivation of the excess surface charge screens effectively the internal polarization of the ferroelectric displacements and is more favorable than free carrier compensation through band bending, also yielding improved stability of the polar slab. In ongoing work, we are exploring the reciprocal effect to understand how the optimal surface composition can influence the stability of ferroelectric polarization across the entire thickness of HfO_2 films (as was predicted recently for ferroelectric $BaTiO_3$ and $PbTiO_3$ [77]).

Our results, in the conjunction with prior work on ferroelectric HfO_2, highlight the importance of the interaction between surface composition and stability of surface polarization. As surfaces and interfaces play emphasized dominant role at small scales, this points to the necessity to consider carefully the role of chemistry and surface engineering in the stabilization and implementation of ferroelectric HfO_2 for technological applications.

Acknowledgements.

JPC and AA acknowledge support from the National Science Foundation (NSF) through Cooperative Agreement Award No. EEC-1160504 for Solicitation NSF 11–537 (TANMS). EAC acknowledges financial support from UCLA for this project. This work used computational and storage services associated with the Hoffman2 Shared Cluster provided by UCLA Institute for Digital Research and Education's Research Technology Group.

References

[1] Z. Fan, J. Chen, and J. Wang, Ferroelectric HfO_2-based materials for next-generation ferroelectric memories, J. Adv. Dielectr. **6**, 1630003 (2016).

[2] T. Mikolajick, S. Slesazeck, M. H. Park, and U. Schroeder, Ferroelectric hafnium oxide for ferroelectric random-access memories and ferroelectric field-effect transistors, MRS Bull. **43**, 340 (2018).

[3] E. Yurchuk, J. Müller, J. Paul, T. Schlösser, D. Martin, R. Hoffmann, S. Müeller, S. Slesazeck, U. Schröeder, and R. Boschke, Impact of scaling on the performance of HfO_2-based ferroelectric field effect transistors, IEEE Trans. Electron Devices **61**, 3699 (2014).

[4] S. S. Cheema, D. Kwon, N. Shanker, R. Dos Reis, S.-L. Hsu, J. Xiao, H. Zhang, R. Wagner, A. Datar, and M. R. McCarter, Enhanced ferroelectricity in ultrathin films grown directly on silicon, Nature **580**, 478 (2020).

[5] P. Polakowski, S. Riedel, W. Weinreich, M. Rudolf, J. Sundqvist, K. Seidel, and J. Muller, in *2014 IEEE 6th International Memory Workshop (IMW)* (IEEE, 2014), pp. 1.

[6] H.-J. Lee, M. Lee, K. Lee, J. Jo, H. Yang, Y. Kim, S. C. Chae, U. Waghmare, and J. H. Lee, Scale-free ferroelectricity induced by flat phonon bands in HfO_2, Science **369**, 1343 (2020).

[7] M. H. Park, Y. H. Lee, H. J. Kim, Y. J. Kim, T. Moon, K. D. Kim, J. Mueller, A. Kersch, U. Schroeder, and T. Mikolajick, Ferroelectricity and antiferroelectricity of doped thin HfO_2-based films, Adv. Mater. **27**, 1811 (2015).

[8] X. Sang, E. D. Grimley, T. Schenk, U. Schroeder, and J. M. LeBeau, On the structural origins of ferroelectricity in HfO_2 thin films, Appl. Phys. Lett. **106**, 162905 (2015).

[9] T. D. Huan, V. Sharma, G. A. Rossetti Jr, and R. Ramprasad, Pathways towards ferroelectricity in hafnia, Phys. Rev. B **90**, 064111 (2014).

[10] R. Batra, T. D. Huan, J. L. Jones, G. Rossetti Jr, and R. Ramprasad, Factors favoring ferroelectricity in hafnia: A first-principles computational study, J. Phys. Chem. **121**, 4139 (2017).

[11] X. Xu, F.-T. Huang, Y. Qi, S. Singh, K. M. Rabe, D. Obeysekera, J. Yang, M.-W. Chu, and S.-W. Cheong, Kinetically stabilized ferroelectricity in bulk single-crystalline HfO_2:Y, Nat. Mater., 1 (2021).

[12] Y. Qi and K. M. Rabe, Phase competition in HfO_2 with applied electric field from first principles, Phys. Rev. B **102**, 214108 (2020).

[13] Y. Qi, S. Singh, C. Lau, F.-T. Huang, X. Xu, F. J. Walker, C. H. Ahn, S.-W. Cheong, and K. M. Rabe, Stabilization of Competing Ferroelectric Phases of HfO_2 under Epitaxial Strain, Phys. Rev. Lett. **125**, 257603 (2020).

[14] Y. Wei, P. Nukala, M. Salverda, S. Matzen, H. J. Zhao, J. Momand, A. S. Everhardt, G. Agnus, G. R. Blake, and P. Lecoeur, A rhombohedral ferroelectric phase in epitaxially strained $Hf_{0.5}Zr_{0.5}O_2$ thin films, Nat. Mater. **17**, 1095 (2018).

[15] R. Materlik, C. Künneth, and A. Kersch, The origin of ferroelectricity in $Hf_{1-x}Zr_xO_2$: A computational investigation and a surface energy model, J. Appl. Phys. **117**, 134109 (2015).

[16] R. Batra, T. D. Huan, G. A. Rossetti Jr, and R. Ramprasad, Dopants promoting ferroelectricity in Hafnia: Insights from A comprehensive chemical space exploration, Chem. Mater. **29**, 9102 (2017).

[17] D. Zhou, J. Müller, J. Xu, S. Knebel, D. Bräuhaus, and U. Schröder, Insights into electrical characteristics of silicon doped hafnium oxide ferroelectric thin films, Appl. Phys. Lett. **100**, 082905 (2012).

[18] M. Falkowski, C. Künneth, R. Materlik, and A. Kersch, Unexpectedly large energy variations from dopant interactions in ferroelectric HfO_2 from high-throughput ab initio calculations, NPJ Comput. Mater. **4**, 1 (2018).

[19] Y. Zhou, Y. Zhang, Q. Yang, J. Jiang, P. Fan, M. Liao, and Y. Zhou, The effects of oxygen vacancies on ferroelectric phase transition of HfO_2-based thin film from first-principle, Comput. Mater. Sci. **167**, 143 (2019).

[20] L. Baumgarten, T. Szyjka, T. Mittmann, M. Materano, Y. Matveyev, C. Schlueter, T. Mikolajick, U. Schroeder, and M. Müller, Impact of vacancies and impurities on ferroelectricity in PVD-and ALD-grown HfO_2 films, Appl. Phys. Lett. **118**, 032903 (2021).

[21] T. Mittmann, M. Materano, P. D. Lomenzo, M. H. Park, I. Stolichnov, M. Cavalieri, C. Zhou, C. C. Chung, J. L. Jones, and T. Szyjka, Origin of ferroelectric phase in undoped HfO_2 films deposited by sputtering, Adv. Mater. Interfaces **6**, 1900042 (2019).

[22] M. Pešić, F. P. G. Fengler, L. Larcher, A. Padovani, T. Schenk, E. D. Grimley, X. Sang, J. M. LeBeau, S. Slesazeck, and U. Schroeder, Physical mechanisms behind the field- cycling behavior of HfO_2- based ferroelectric capacitors, Adv. Funct. Mater. **26**, 4601 (2016).

[23] S. V. Barabash, D. Pramanik, Y. Zhai, B. Magyari-Kope, and Y. Nishi, Ferroelectric switching pathways and energetics in (Hf, Zr)O_2, ECS Trans. **75**, 107 (2017).

[24] R. Materlik, C. Künneth, and A. Kersch, The origin of ferroelectricity in $Hf_{1-x}Zr_xO_2$: A computational investigation and a surface energy model, J. Appl. Phys. **117**, 134109 (2015).

[25] R. Batra, H. D. Tran, and R. Ramprasad, Stabilization of metastable phases in hafnia owing to surface energy effects, Appl. Phys. Lett. **108**, 172902 (2016).

[26] W. Hamouda, A. Pancotti, C. Lubin, L. Tortech, C. Richter, T. Mikolajick, U. Schroeder, and N. Barrett, Physical chemistry of the TiN/$Hf_{0.5}Zr_{0.5}O_2$ interface, J. Appl. Phys. **127**, 064105 (2020).

[27] P. D. Lomenzo, Q. Takmeel, C. Zhou, C. M. Fancher, E. Lambers, N. G. Rudawski, J. L. Jones, S. Moghaddam, and T. Nishida, TaN interface properties and electric field cycling effects on ferroelectric Si-doped HfO_2 thin films, J. Appl. Phys. **117**, 134105 (2015).

[28] R. Athle, A. E. Persson, A. Irish, H. Menon, R. Timm, and M. Borg, Effects of TiN Top Electrode Texturing on Ferroelectricity in $Hf_{1-x}Zr_xO_2$, ACS Appl. Electron. Mater. **13**, 11089 (2021).

[29] M. H. Park, H. J. Kim, Y. J. Kim, W. Jeon, T. Moon, and C. S. Hwang, Ferroelectric properties and switching endurance of $Hf_{0.5}Zr_{0.5}O_2$ films on TiN bottom and TiN or RuO_2 top electrodes, Phys. Stat. Sol. RRL. **8**, 532 (2014).

[30] T. Szyjka, L. Baumgarten, T. Mittmann, Y. Matveyev, C. Schlueter, T. Mikolajick, U. Schroeder, and M. Müller, Enhanced ferroelectric polarization in TiN/HfO_2/TiN capacitors by interface design, ACS Appl. Electron. Mater. **2**, 3152 (2020).

[31] S. S. Fields, S. W. Smith, C. M. Fancher, M. D. Henry, S. L. Wolfley, M. G. Sales, S. T. Jaszewski, M. A. Rodriguez, G. Esteves, and P. S. Davids, Metal Nitride Electrode Stress and Chemistry Effects on Phase and Polarization Response in Ferroelectric $Hf_{0.5}Zr_{0.5}O_2$ Thin Films, Adv. Mater. Interfaces, 2100018 (2021).

[32] S. Starschich, S. Menzel, and U. Böttger, Evidence for oxygen vacancies movement during wake-up in ferroelectric hafnium oxide, Appl. Phys. Lett. **108**, 032903 (2016).

[33] S. S. Fields, S. W. Smith, P. J. Ryan, S. T. Jaszewski, I. A. Brummel, A. Salanova, G. Esteves, S. L. Wolfley, M. D. Henry, and P. S. Davids, Phase-Exchange-Driven Wake-Up and Fatigue in Ferroelectric Hafnium Zirconium Oxide Films, ACS Appl. Electron. Mater. **12**, 26577 (2020).

[34] M. Hoffmann, U. Schroeder, T. Schenk, T. Shimizu, H. Funakubo, O. Sakata, D. Pohl, M. Drescher, C. Adelmann, and R. Materlik, Stabilizing the ferroelectric phase in doped hafnium oxide, J. Appl. Phys. **118**, 072006 (2015).

[35] K. Garrity, A. Kakekhani, A. Kolpak, and S. Ismail-Beigi, Ferroelectric surface chemistry: First-principles study of the $PbTiO_3$ surface, Phys. Rev. B **88**, 045401 (2013).

[36] S. V. Levchenko and A. M. Rappe, Influence of ferroelectric polarization on the equilibrium stoichiometry of lithium niobate (0001) surfaces, Phys. Rev. Lett. **100**, 256101 (2008).

[37] D. Fong, A. Kolpak, J. Eastman, S. Streiffer, P. Fuoss, G. Stephenson, C. Thompson, D. Kim, K. J. Choi, and C. Eom, Stabilization of monodomain polarization in ultrathin $PbTiO_3$ films, Phys. Rev. Lett. **96**, 127601 (2006).

[38] G. Kresse and J. Furthmüller, Efficient iterative schemes for ab initio total-energy calculations using a plane-wave basis set, Phys. Rev. B **54**, 11169 (1996).

[39] J. P. Perdew, K. Burke, and M. Ernzerhof, Generalized gradient approximation made simple, Phys. Rev. Lett. **77**, 3865 (1996).

[40] H. J. Monkhorst and J. D. Pack, Special points for Brillouin-zone integrations, Phys. Rev. B **13**, 5188 (1976).

[41] P. E. Blöchl, Projector augmented-wave method, Phys. Rev. B **50**, 17953 (1994).

[42] See Supplemental Material at [URL will be inserted by publisher] for the bulk orthorhombic HfO_2 total energy convergence with respect to *k*-point density and planewave kinetic energy cut-off, lattice parameters and phonon and electronic densities of states of the bulk tetragonal and orthorhombic phases, additional structural and electronic characterizations of the three lowest energy surfaces, comparison between DFT-PBE- and DFT-SCAN-predicted phase-transition enthalpies among various HfO_2 solid phases, surface vibrational frequencies of select surfaces, Shomate equation constants for O_2 gas, and surfaces energies of all the sampled compositions for both tetragonal and orthorhombic slabs at 900 K and 1 bar O_2.

[43] S. C. Pandey, X. Xu, I. Williamson, E. B. Nelson, and L. Li, Electronic and vibrational properties of transition metal-oxides: Comparison of GGA, GGA+ U, and hybrid approaches, Chem. Phys. Lett. **669**, 1 (2017).

[44] J. P. Perdew and M. Levy, Physical content of the exact Kohn-Sham orbital energies: band gaps and derivative discontinuities, Phys. Rev. Lett. **51**, 1884 (1983).

[45] L. J. Sham and M. Schlüter, Density-functional theory of the energy gap, Phys. Rev. Lett. **51**, 1888 (1983).

[46] H. Yu, M. Li, B. J. Cho, C. Yeo, M. Joo, D.-L. Kwong, J. Pan, C. Ang, J. Zheng, and S. Ramanathan, Energy gap and band alignment for $(HfO_2)_x(Al_2O_3)_{1-x}$ on (100) Si, Appl. Phys. Lett. **81**, 376 (2002).

[47] W. Zhu, T. Tamagawa, M. Gibson, T. Furukawa, and T. Ma, Effect of Al inclusion in HfO_2 on the physical and electrical properties of the dielectrics, IEEE Trans. Electron Devices **23**, 649 (2002).

[48] N. V. Nguyen, S. Sayan, I. Levin, J. R. Ehrstein, I. J. R. Baumvol, C. Driemeier, C. Krug, L. Wielunski, P. Y. Hung, and A. Diebold, Optical band gaps and composition dependence of hafnium–aluminate thin films grown by atomic layer chemical vapor deposition, J. Vac. Sci. Technol. **23**, 1706 (2005).

[49] M. Modreanu, P. Hurley, B. O'Sullivan, B. O'Looney, J.-P. Senateur, H. Rousell, F. Rousell, M. Audier, C. Dubourdieu, and I. W. Boyd, in *Opto-Ireland 2002: Optics and Photonics Technologies and Applications* (International Society for Optics and Photonics, 2003), pp. 1236.

[50] R. Eglitis, J. Purans, and R. Jia, Comparative Hybrid Hartree-Fock-DFT Calculations of WO_2-Terminated Cubic WO_3 as Well as $SrTiO_3$, $BaTiO_3$, $PbTiO_3$ and $CaTiO_3$ (001) Surfaces, Crystals **11**, 455 (2021).

[51] R. I. Eglitis, Comparative first-principles calculations of $SrTiO_3$, $BaTiO_3$, $PbTiO_3$ and $CaTiO_3$ (001), (011) and (111) surfaces, Ferroelectrics **483**, 53 (2015).

[52] P. Ondračka, D. Holec, D. Nečas, and L. Zajíčková, Accurate prediction of band gaps and optical properties of HfO_2, J. Phys. D: Appl. Phys. **49**, 395301 (2016).

[53] M. Grüning, R. Shaltaf, and G.-M. Rignanese, Quasiparticle calculations of the electronic properties of ZrO_2 and HfO_2 polymorphs and their interface with Si, Phys. Rev. B **81**, 035330 (2010).

[54] K. Reuter and M. Scheffler, Composition, structure, and stability of RuO_2 (110) as a function of oxygen pressure, Phys. Rev. B **65**, 035406 (2001).

[55] B. d. Darwent, Bond dissociation energies in simple molecules, (US National Bureau of Standards, Washington, DC, 1970).

[56] D. R. Burgess, Jr., Thermochemical Data in *NIST Chemistry WebBook*, NIST Standard Reference Database Number 69, edited by P. J. Linstrom and W. G. Mallard (National Institute of Standards and Technology, Gaithersburg, MD, 2009), http://webbook.nist.gov.

[57] E. D. Grimley, T. Schenk, T. Mikolajick, U. Schroeder, and J. M. LeBeau, Atomic structure of domain and interphase boundaries in ferroelectric HfO_2, Adv. Mater. Interfaces **5**, 1701258 (2018).

[58] K. Momma and F. J. J. o. a. c. Izumi, VESTA 3 for three-dimensional visualization of crystal, volumetric and morphology data, J. Appl. Crystallogr. **44**, 1272 (2011).

[59] J. Woo, Y. Goh, S. Im, J. H. Hwang, Y. Kim, J. H. Kim, J.-P. Im, S.-M. Yoon, S. E. Moon, and S. Jeon, Improved Ferroelectric Switching in Sputtered $HfZrO_x$ Device Enabled by High Pressure Annealing, IEEE Trans. Electron Devices **41**, 232 (2019).

[60] H. A. Hsain, Y. Lee, G. Parsons, and J. L. Jones, Compositional dependence of crystallization temperatures and phase evolution in hafnia-zirconia $(Hf_xZr_{1-x})O_2$ thin films, Appl. Phys. Lett. **116**, 192901 (2020).

[61] M. H. Park, C. C. Chung, T. Schenk, C. Richter, K. Opsomer, C. Detavernier, C. Adelmann, J. L. Jones, T. Mikolajick, and U. Schroeder, Effect of Annealing Ferroelectric HfO_2 Thin Films: In Situ, High Temperature X- Ray Diffraction, Adv. Electron. Mater. **4**, 1800091 (2018).

[62] P. Tasker, The stability of ionic crystal surfaces, J. Phys. C: Solid State Phys. **12**, 4977 (1979).

[63] M. Setvin, M. Reticcioli, F. Poelzleitner, J. Hulva, M. Schmid, L. A. Boatner, C. Franchini, and U. Diebold, Polarity compensation mechanisms on the perovskite surface $KTaO_3$ (001), Science **359**, 572 (2018).

[64] C. Gattinoni, N. Strkalj, R. Härdi, M. Fiebig, M. Trassin, and N. A. Spaldin, Interface and surface stabilization of the polarization in ferroelectric thin films, Proc. Natl. Acad. Sci. U.S.A. **117**, 28589 (2020).

[65] M. Stengel, Electrostatic stability of insulating surfaces: Theory and applications, Phys. Rev. B **84**, 205432 (2011).

[66] C. J. Cramer, W. B. Tolman, K. H. Theopold, and A. L. Rheingold, Variable character of O—O and M—O bonding in side-on (η^2) 1:1 metal complexes of O_2, Proc. Natl. Acad. Sci. U.S.A. **100**, 3635 (2003).

[67] G. Henkelman, A. Arnaldsson, and H. Jónsson, A fast and robust algorithm for Bader decomposition of charge density, Comput. Mater. Sci. **36**, 354 (2006).

[68] R. Bader, *Atoms in Molecules: A Quantum Theory Oxford University* Press: Oxford, nº UK, 1990).

[69] B. Huang, Y. Chen, Y.-P. Chiu, Y. Huang, J. Yang, Y. Chen, and Y. Chu, Direct observation of ferroelectric polarization-modulated band bending at oxide interfaces, Appl. Phys. Lett. **100**, 122903 (2012).

[70] R. E. Cohen, Surface effects in ferroelectrics: Periodic slab computations for $BaTiO_3$, Ferroelectrics **194**, 323 (1997).

[71] J. He, G. Stephenson, and S. Nakhmanson, Electronic surface compensation of polarization in $PbTiO_3$ films, J. Appl. Phys. **112**, 054112 (2012).

[72] S. V. Kalinin, Y. Kim, D. D. Fong, and A. N. Morozovska, Surface-screening mechanisms in ferroelectric thin films and their effect on polarization dynamics and domain structures, Rep. Prog. Phys. **81**, 036502 (2018).

[73] P. Buragohain, C. Richter, T. Schenk, H. Lu, T. Mikolajick, U. Schroeder, and A. Gruverman, Nanoscopic studies of domain structure dynamics in ferroelectric La:HfO_2 capacitors, Appl. Phys. Lett. **112**, 222901 (2018).

[74] D. Zhou, J. Xu, Q. Li, Y. Guan, F. Cao, X. Dong, J. Müller, T. Schenk, and U. Schröder, Wake-up effects in Si-doped hafnium oxide ferroelectric thin films, Appl. Phys. Lett. **103**, 192904 (2013).

[75] T. Schenk, M. Hoffmann, J. Ocker, M. Pešić, T. Mikolajick, and U. Schroeder, Complex internal bias fields in ferroelectric hafnium oxide, ACS Appl. Electron. Mater. **7**, 20224 (2015).

[76] P. Jiang, Q. Luo, X. Xu, T. Gong, P. Yuan, Y. Wang, Z. Gao, W. Wei, L. Tai, and H. Lv, Wake- Up Effect in HfO_2- Based Ferroelectric Films, Adv. Electron. Mater. **7**, 2000728 (2021).

[77] W. A. Saidi, J. M. P. Martirez, and A. M. Rappe, Strong reciprocal interaction between polarization and surface stoichiometry in oxide ferroelectrics, Nano Lett. **14**, 6711 (2014).

[78] J. J. Low, N. H. Paulson, M. D'Mello, and M. Stan, Thermodynamics of monoclinic and tetragonal hafnium dioxide (HfO_2) at ambient pressure, CALPHAD 72, 102210 (2021).

[79] I. MacLaren, T. Ras, M. MacKenzie, A. Craven, D. McComb, and S. De Gendt, Texture, twinning, and metastable “tetragonal” phase in ultrathin films of HfO_2 on a Si substrate, J. Electrochem. Soc. 156, G103 (2009).

[80] B. Sklénard, A. Dragoni, F. Triozon, and V. Olevano, Optical vs electronic gap of hafnia by ab initio Bethe-Salpeter equation, Appl. Phys. Lett. 113, 172903 (2018).

[81] J. Beltrán, M. Muñoz, and J. Hafner, Structural, electronic and magnetic properties of the surfaces of tetragonal and cubic HfO_2, New J. Phys. 10, 063031 (2008).

[82] J. Sun, R. C. Remsing, Y. Zhang, Z. Sun, A. Ruzsinszky, H. Peng, Z. Yang, A. Paul, U. Waghmare, and X. Wu, Accurate first-principles structures and energies of diversely bonded systems from an efficient density functional, Nat. Chem. 8, 831 (2016).

[83] A. Togo and I. Tanaka, First principles phonon calculations in materials science, Scr. Mater. 108, 1 (2015).

[84] C. Wang, M. Zinkevich, and F. Aldinger, The zirconia–hafnia system: DTA measurements and thermodynamic calculations, J. Am. Ceram. Soc. 89, 3751 (2006).

[85] X. Luo, W. Zhou, S. V. Ushakov, A. Navrotsky, and A. A. Demkov, Monoclinic to tetragonal transformations in hafnia and zirconia: A combined calorimetric and density functional study, Phys. Rev. B 80, 134119 (2009).

[86] T. A. Lee and A. Navrotsky, Enthalpy of formation of cubic yttria-stabilized hafnia, J. Mater. Res. 19, 1855 (2004).